

Alternative approach on an in-situ analysis of the thermal progression during the LPBF-M process using welded thermocouples embedded into the substrate plate

N.Schnell^A, M.Siewert^B, S.Kleszczynski^A, G.Witt^A, V.Ploshikhin^B

^A *University of Duisburg-Essen, Chair of Manufacturing Technology, Germany*

^B *University of Bremen, BCCMS/ISEMP, Germany*

Abstract

Laser powder bed fusion (LPBF-M) is a very potent technology for creating highly individualized, complex, and functional metal parts. One of the major influencing factors is the thermal progression. It significantly determines size accuracy, microstructure and process stability. Therefore, creating an enhanced understanding of thermal phenomena through measurements and simulations is crucial to increase the reliability of the technology. Current research is mainly based on temperature measurements of the upper layer, leaving major scope for the conditions at the substrate-part-interface. This area is of utmost technical importance because it serves as the main heat sink. Insufficient heat dissipation leads to accumulations of heat, deformations, and process breakdowns. This contribution presents a simple and flexible method to analyze the thermal progression close to the part inside the substrate plate. The acquired data shows very high consistency. Additionally, the results are compared to a model created using an ISEMP developed FEM-Software which shows promising results for validation studies.

Keywords: Laser Powder Bed Fusion of Metals (LPBF-M), Thermocouple, Finite element modeling (FEM), Validation, Thermocouple, Stainless steel 1.4542 (GP1)

1. Introduction

The laser powder bed fusion of metals (LPBF-M) process has gained a lot of attention in research and industry during the last decade and creates an increasing number of industrial business cases. It enables building-up complex metallic parts in a one-step process. The potential for individual, geometrically functional and optimized parts through the layerwise build up principle has been proven in multiple studies [1–3] and led to immense growth in this business sector [4].

One of the primary advantages of the LPBF-M process is the possibility to use innovative new materials with tailored properties as well as build complex and demanding structures. However, this poses one of the biggest challenges for this technology. Many promising materials, like maraging steel (MS1), high entropy alloys, and amorphous metals, are very sensitive towards their thermal history [5, 6]. Fur-

thermore, especially for complex geometries, an effect of superelevation can occur during the building process caused by heat accumulation [7–9]. The energy used to melt the powder needs to be dissipated mainly through previously solidified material because metal powder has an around 100 times lower thermal conductivity than solid material [10–12]. Therefore, developing a better understanding of the thermal processes during LPBF-M is essential to enhance its stability and reproducibility.

State of the art

Grasso et al.[13] summarise many publications on in-situ process monitoring for LPBF-M. Since powder bed and recoating system strongly complicate accessibility the current state of research is mainly based on the usage of thermal cameras or pyrometry, observing temperatures only in the upper layer [14, 15]. This approach, although costly, can provide very valuable insight. Nevertheless, in most cases, it can only generate relative temperatures due to its high reliance on accurate emissivity values. These, on the other hand, are very complex to determine because of rapid temperature and phase changes during the melting process. Therefore, thermal cameras are an unreliable source for validating simulations [16]. The top layer experiences multiple phenomena like melting, recrystallization, evaporation or the Marangoni effect interacting with each other creating a highly complex thermal system. Hence, the data gained from the measurements consists of many causalities overlapping each other, complicating their interpretation [17].

A simpler method to gain in-situ temperature data is to use thermocouples from below the substrate plate. Here, only the heat dissipation from part to plate is the most dominant influencing factor. However, the plate itself has a very high tare volume, causing severe thermal inertia. Therefore, since fluctuation between heating through the laser and cooling during recoating are such a decisive characteristic for the process, the thermal inertia needs to be reduced to increase measurement resolution. This can be done by reducing the thickness of the substrate plate to be able to measure closer to the part. Dunbar et al.[18] have used this approach for residual stress measurements. They were able to clearly resolve heating and cooling cycles in regards to the distortion. However, the massive vault they used in their setup fills the whole building platform and is comparably costly. Additionally, thinning the substrate plate leads to strong deviations from the regular process because the characteristics of the plate as a heat sink significantly rely on its tare volume. Jhabvala et al.[19] have performed a similar experiment with five thermocouples on a 5 mm x 5 mm platelet using highly conductive gold powder focusing on scanning strategies. They managed to measure the temperature progression over a range of ~1000 °C, evaluated different scan strategies and accurately fitted the results to a FEM-Simulation. Peyre et al.[20] used spot welded thermocouples to analyze the DED (Direct energy deposition) process. It is more accessible so that the thermocouples could be positioned very close to the first scan line. They did not influence the thermal system and could directly develop and validate a very process-oriented simulation out of their data. For this work, a setup was designed that also uses spot welded thermocouples to measure the

temperature during the building process. A simple redesign of the substrate plate was made to enable measurements with only 2 mm distance to the part. Hence, it reaches a very high resolution while largely keeping the integrity of the thermal system of the substrate plate.

2. Experimental System

The experiments were conducted using an EOS M290 LPBF-M machine with modified substrate and base plates as well as an integrated additional temperature sensor system. A regular substrate plate has a surface area of 250 x 250 mm. Here, a C45 steel substrate plate of 220 mm x 220 mm was fixated on an adapter ring with minimal contact area. The base plate used has a recess, so that wiring for the thermocouples can be led from below the substrate plate through the shaft of the building platform.

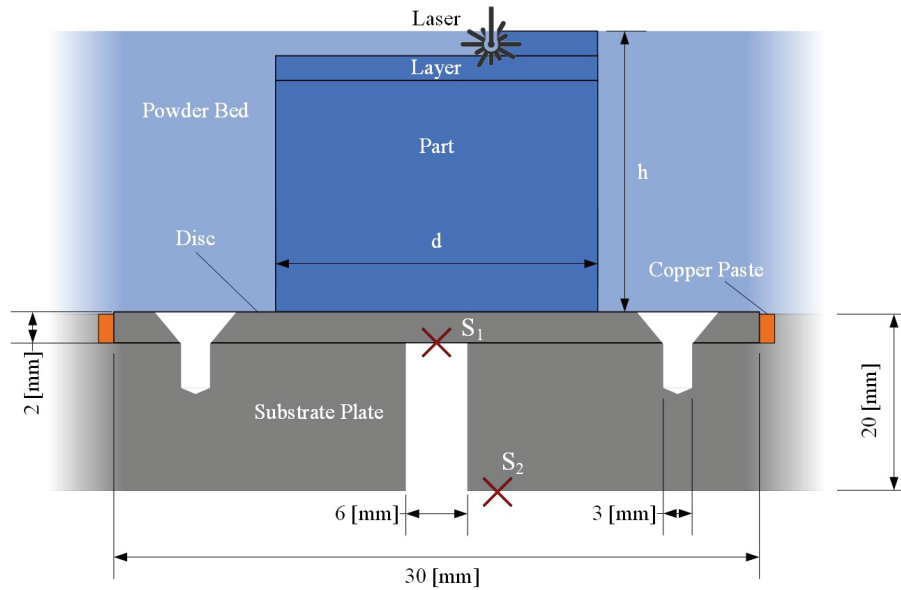


Figure 1: Schematic close up of the additive part on the disc positioned in the slot within the substrate plate. The sensors **S1** and **S2**, the diameter **d**, and the height **h** of the part are depicted. The disc is thermally connected to the substrate plate through a film of copper paste.

Substrate Plate

A close up on the modifications of the substrate plate is depicted in figure 1. A circular slot of 30.5 mm diameter and 1.9 mm depth was milled into the center of the plate. A 5 mm diameter hole was drilled through the plate in the center of the slot for wiring of the thermocouple. To fixate a 2 mm strong disc with a diameter of 30 mm, two additional holes were drilled and threaded for 6 mm long M3 screws. Analogously to the substrate plate itself, the disc was made from regular C45 steel ($\lambda_{C45}(20\text{ }^{\circ}\text{C}) = 43\text{ W/m}\cdot\text{K}$). To ensure comparable heat conduction, the gap between the side of the disc and the plate was thermally bridged using a conventional copper paste with a heat conductivity $\lambda_{CuP}(20\text{ }^{\circ}\text{C}) \approx 200\text{ W/m}\cdot\text{K}$ (Components: Cu, SiO₂, SiO, C₁₅H₂₄O).

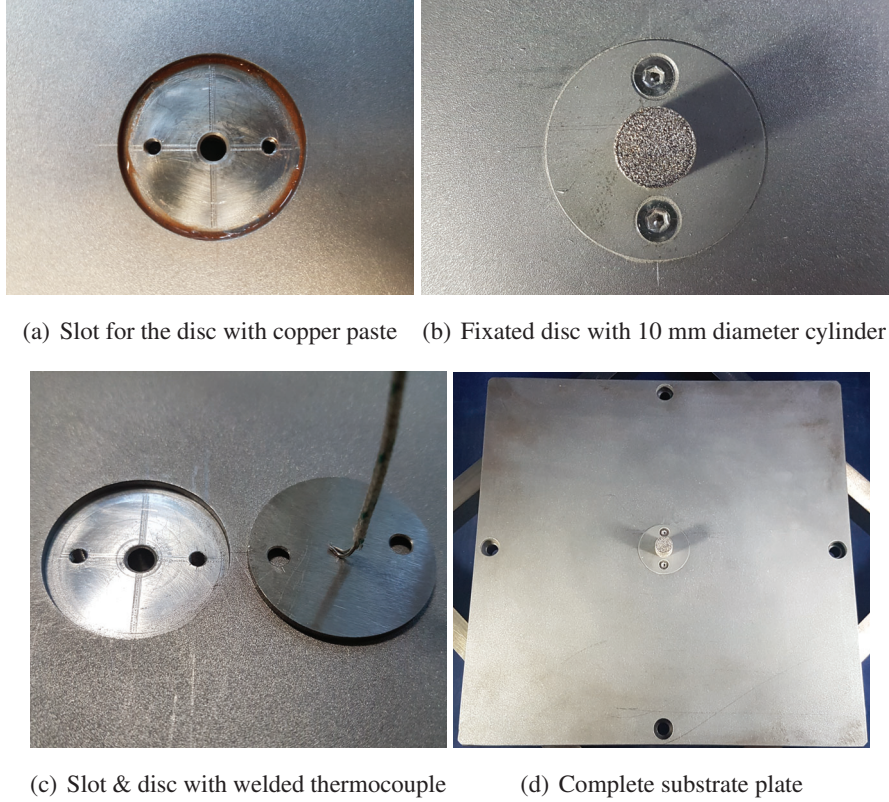


Figure 2: Pictures of the slot within the substrate plate with one hole for the thermocouple in the center and two holes for fixation with M3 screws **(a)**, close up on fixated disc after the building process of a $d = 10$ mm cylinder **(b)**, disc with two holes for fixation and spot welded K-type thermocouple **(c)**, complete substrate plate ($220 \times 220 \times 20 \text{ mm}$) with fixated disc **(d)**.

Temperature sensor system

As shown in figure 1, two sensors were integrated into the setup. Both were welded from K-type thermocouple (Cr-Ni) wire using a spot welder. Sensor 1 (**S1**) was additionally spot welded directly onto the disc (Figure 2(c)), ensuring maximum resolution through minimum tare volume, and thus minimal thermal inertia. A Testo 635 with an accuracy of $0.3 \text{ }^{\circ}\text{C}$ was used to read out the data. Sensor 2 (**S2**) had the purpose to measure an averaged temperature of the substrate plate and serve as a reference value for the simulation. Since the substrate plate has a much higher tare volume, compared to disc and part, the temperature progression is comparably slower. Therefore, the requirement for resolution was lower for sensor 2 and it was read out using an Arduino Uno micro-controller with a MAX6675 as a cold-junction-compensated digital converter. This setup has a resolution of $0.25 \text{ }^{\circ}\text{C}$, an accuracy of $1 - 2 \text{ }^{\circ}\text{C}$ and is fairly sensitive to ground contact and different potentials. Hence, sensor 2 had to be galvanically insulated from the substrate plate using insulating tape. For post-processing, the data from sensor 2 was smoothed using a moving average function. Both sensors were read out once per second.

Process parameter

The material GP1 (1.4542 / 17-4PH: Cr 15-17.5 wt%, Ni 3-5 wt%, Cu 3-5 wt%)[21] was chosen. It is well researched and has a broad number of applications. The process parameters laser power ($P = 190$ W), laser velocity ($v = 1150 \frac{\text{mm}}{\text{s}}$) and hatch distance ($a = 0.09$ mm) were used for maximum process stability according to previous optimization studies. All other assist parameters, like contour or up-/downskin, were switched off because their implementation into the simulation is rather complex and has no significant benefit to the experiment. The only exceptions are the skywriting parameter, which was kept active to ensure a constant velocity for the exposure and rotating scan patterns, for more uniform energy deposition.

The part geometries that were chosen are defined by the limited space of the disc and are kept simple to ensure a stable process. Additionally, radial symmetrical shapes were used to reduce computing times of the simulation. Therefore, a cylinder with a diameter of 10 mm and a height of 10 mm was picked as a benchmark. It was compared to a smaller cylinder of 5 mm diameter and cones with a diameter progression of 10 mm \rightarrow 5 mm and 5 mm \rightarrow 10 mm.

3. Simulation

In addition to experimental investigations, numerical process simulations are a valuable tool to analyze process behaviour. Whereas measurements are usually restricted to a certain number of measurement points, simulation models can provide values everywhere in the considered domain of interest. After modeling and implementation, a finalized simulation method can be used with little effort to perform numerous numerical experiments and provides many opportunities for process optimization. Since simulations are based on assumptions and approximations, validation and calibration with experimental data is always an essential task. A combination of simulation and experimental work can lead to reliable results and deepen the insight into the process.

For this investigation, a macroscopic approach is used. The model is expected to predict the global part heat-up and the temperatures in the substrate plate well. It is based on the simplification that the laser energy is instantaneously absorbed into the system without including melting or solidification of the material. After adding a new layer of solid material at a prescribed temperature, the cool-down is calculated. This procedure is repeated until all layers are added. A formal formulation and its numerical treatment will be given in the following paragraphs.

Simulation model

Let $[0, T)$ denote the time interval of the overall process and consider its decomposition into sub-intervals $[0, T) = \bigcup_{i=0}^N [t_i, t_{i+1})$, where each sub-interval $[t_i, t_{i+1})$ corresponds to the build up time of one layer including coating and exposure of the powder. The spatial domain $\Omega(t) \subset \mathbb{R}^3$, which describes the already exposed solid material as well as the substrate plate, evolves in time due to the material addition in LPBF-M processes. It is assumed that $\Omega(t)$ is constant on each interval (t_i, t_{i+1}) and the addition of material happens instantaneously at time t_i , i.e. $\Omega(t) = \Omega_i := \bigcup_{k=0}^i P_k \cup S$ for $t \in [t_i, t_{i+1})$, whereby S describes the geometry of the substrate plate and P_k of the part layer k . The simulation model is based on the well known *heat equation*, which arises from combining energy balance with *Fourier's law*. For a prescribed *activation temperature* θ_{act} and *room temperature* θ_{room} the temperature functions $\theta_i : \Omega_i \times [t_i, t_{i+1}] \rightarrow \mathbb{R}$ on each sub-time-interval are determined as solution of the following sequence of initial-boundary value problems and define the overall temperature function $\theta : \Omega(t) \times [0, T) \rightarrow \mathbb{R}$ by $\theta(r, t) = \theta_i(r, t)$ if $t \in [t_i, t_{i+1})$:

$$\begin{cases} \rho c_p \partial_t \theta_i - \nabla \cdot (\lambda \nabla \theta_i) = 0 & \text{in } \Omega_i \times [t_i, t_{i+1}], \\ \nabla \theta_i(r, t) \cdot n = 0 & \text{for } (r, t) \in \partial \Omega_i \times (t_i, t_{i+1}), \\ \theta_i(r, t_i) = \theta_i^{\text{init}}(r) & \text{for } r \in \Omega_i, \end{cases} \quad (1)$$

where

$$\theta_{-1}^{\text{init}}(r) = \theta_{\text{room}} \text{ for } r \in \Omega_{-1} = S \text{ and } \theta_i^{\text{init}}(r) = \begin{cases} \theta_{i-1}(r, t_i) & \text{if } r \in \Omega_{i-1}, \\ \theta_{\text{act}} & \text{else.} \end{cases}$$

In the above system of equations, ρ denotes the *density*, c_p the *specific heat capacity*, and λ the *thermal conductivity* corresponding to the material. Phase transformation effects are neglected in this macro-model and therefore ρc_p is assumed to be constant with respect to temperature. To include the difference of the substrate plate and part material, ρc_p is chosen differently on S and $\Omega_i \setminus S$. For the same reason, the thermal conductivity λ is also chosen differently for substrate plate and part. Furthermore, the thermal conductivity is known to be temperature dependent. This dependency is taken into account on the part since the part temperature during the process changes several times from room temperature up to melting temperature. On the substrate plate, the thermal conductivity is assumed to be constant.

Note, that only the substrate plate and the part itself is part of $\Omega(t)$, whereas the powder is not. This means that the powder is not directly taken into account. Instead, insulation at the solid-powder interface is assumed. Due to the already mentioned fact that the thermal conductivity of powder is up to 100 times less than the thermal conductivity of solid, the isolation boundary condition at the solid-powder interface is a reasonable simplification.

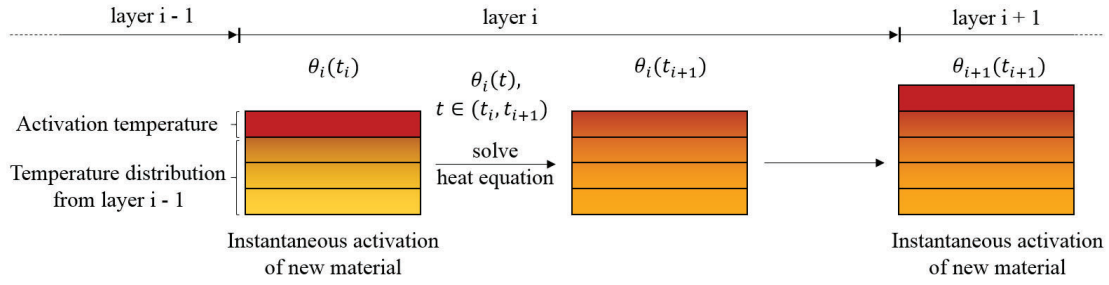


Figure 3: Schematic illustration of the simulation model.

Numerical solution of the simulation model

The model stated above is solved by means of a numerical approximation of its solution. Therefore, (1) is discretised via an *implicit Euler* scheme in time and the *Finite Element Method* (FEM) in space (for more information about solving parabolic equations by FEM see e.g. [22] from a mathematical or [23] from an engineering point of view). If θ_i^h denotes the FEM approximation of θ_i , the discretised initial value $\theta_i^h(t_i)$ for layer i is obtained by projecting the function

$$r \mapsto \begin{cases} \theta_{i-1}^h(r, t_i) & \text{if } r \in \Omega_{i-1}, \\ \theta_{\text{act}} & \text{else.} \end{cases}$$

with respect to the $L^2(\Omega_i)$ norm into the chosen finite element subspace. Note, that assigning the initial values in this way is important, since it ensures that the amount of energy in the system described by the FEM approximation is the same as in the model. If (in case of e.g. Lagrangian FEM with nodal basis functions) one instead sets only the temperatures of new nodes to θ_{act} , the initial temperature $\theta_i^h(t_i)$ in the added layer would strongly depend on the temperature of the underling nodes and the procedure would finally cause an uncontrolled energy input.

Due to symmetry, it is possible to mesh and simulate only a quarter of the whole domain. It consists of unstructured Hex-8 elements and possesses a layerwise structure. The mesh was first generated with help of an algorithm introduced by Kober et al. [24] and then adapted to gain different mesh resolutions, i.e. a fine mesh close to the part and coarse mesh on the substrate plate far away from the path. The layer height in the part region is $40\mu\text{m}$, i.e. two times of the process layer height. Therefore, each FEM layer is split up into two layers with $20\mu\text{m}$ heights, which are activated one after another. Furthermore, an additional split up of each new layer is performed, to increase the accuracy of the initial value projection. After simulating the layers corresponding to one FEM layer, they will be coarsened again. All computations are performed by a FEM software, which was developed at ISEMP.

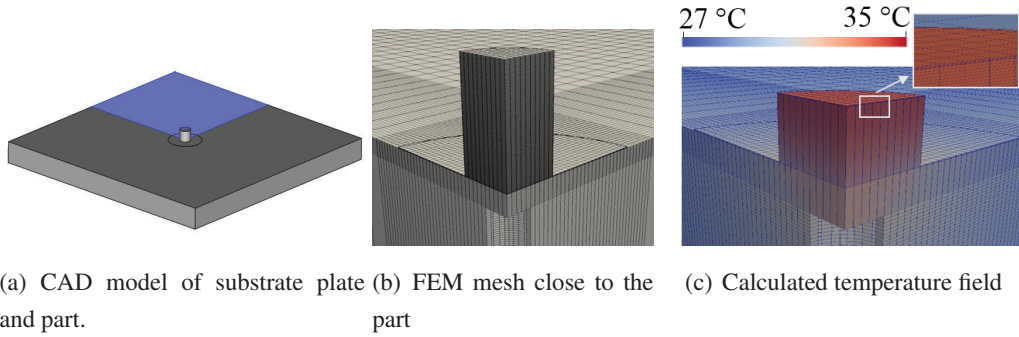


Figure 4: Computational domain, FEM mesh and calculated temperature field of cylindrical sample with $d = 10\text{mm}$; Only the blue colored quarter (a) needs to be considered in the simulation due to symmetry.

Parameters of the simulation model

The difference of activation temperature and room temperature $\theta_{\text{act}} - \theta_{\text{room}}$ defines the amount of absorbed laser-energy per mass, i.e. the energy density, which is inserted in the system if new material is added. The value was fitted, so that the measured peak temperatures of the first layer at S1 of the cylinder sample ($d = 10\text{mm}$) are reproduced correctly. The measured peak temperatures show a high scattering due to a low time resolution (cf. section 4). Therefore, the peak temperature of the first layer was estimated to be 83°C by manually estimating a curve, which connects the measured maximal peak temperatures. The obtained activation energy density is 25.35J/mm^3 , which is used for all samples. Note that the whole energy is inserted in one single layer. It is well known that several underlying layers will be molten during the exposure of a new single layer in LPBF-M processes (this is important to guarantee the connectivity of each new layer to the part and reduce the porosity). Since the energy, which is necessary to melt several layers, in reality, is inserted in the simulation into a single layer by activating it at θ_{act} , it is clear that the resulting temperatures θ_{act} are significantly higher than melt temperature. The material parameters were taken from data sheets (substrate plate material: C45 steel [25], part material: GP1 / 1.4542 steel [21]). Only the specific heat capacity of GP1 / 1.4542 steel was generated with the help of the JMatPro software since it was not provided. The temperature dependent function of thermal conductivity is defined as a linear inter-/extrapolation of the stated values. All used parameters are described in table 1.

		20 °C	100 °C	200 °C	300 °C
λ_{part}	[W/(m K)]	13	14	15	16
$\lambda_{\text{sub-plate}}$	[W/(m K)]	42			
$c_{\rho,\text{part}}$	[J/(kg K)]	500			
$c_{\rho,\text{sub-plate}}$	[J/(kg K)]	470			
ρ_{part}	[kg/m ³]	7800			
$\rho_{\text{sub-plate}}$	[kg/m ³]	7800			

Table 1: Material parameters used for the simulations

The duration to recoat a new powder layer was reported by the used machine to be 9 s. In case of the cylindrical samples the exposure time of each layer was determined by measuring the overall process time. After dividing it by the number of process layers and subtracting the recoating time one obtains the exposure time. This results in 1.2 s for the cylinder with $d = 10$ mm diameter and 0.6 s for the cylinder with $d = 5$ mm diameter. Since first and last layer of the cone samples are equal to one of the cylindrical specimens, the layer exposure time is assumed to be a linear in-/decreasing function of these times in case of the cone samples. Exemplary timing measurements agreed with this assumption.

4. Results

Six different experiments have been conducted to analyze four potential influencing factors on the temperature progression at the connection of the part to the substrate plate: Part volume, interface area to the substrate plate, the influence of the copper paste, layer height. The cooling after the process was also recorded under unaltered conditions without opening the machine.

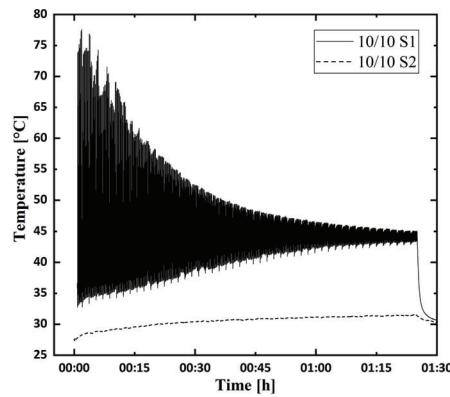


Figure 5: Temperature progression of sensor 1 (S1) 2 mm below the part and sensor 2 (S2) under the substrate plate for the build up of a 10 mm high cylinder with a diameter of 10 mm.

Figure 5 shows the temperature progressions for the build up process of the benchmark cylinder ($d = 10$ mm). The first half minute of data from S1 is missing for this specific experiment due to malfunction. Nevertheless, the average temperature before the experiment was documented and matches the starting temperature of S2 for all experiments only with a deviation of around 0.5 °C.

The characteristic progression of temperature S1 can be seen. It fluctuates with decreasing amplitude until reaching a nearly stable value of around 44.3 °C. This temperature represents the average temperature during the process. Its gradient is closely related to the average temperature in the center of the substrate plate depicted by S2. The amplitude lies between 77.6 and 32.7 °C. These fluctuations emerge from the change between heating during laser exposure (~1.2 s) and cooling during recoating (~9 s). With increasing height, the amplitude is damped because of increasing thermal inertia. A clear development of upper and lower peaks can be seen. The noticeable deviations of some peaks from this progression

can be explained through the temporal resolution of the measurement. This effect is more significant for the maximum peaks because of comparably low laser exposure time in contrast to recoating time. The rapid cooling process after the build up was also recorded. It can be used for fitting the heat loss of the total system in the simulation. However, this approach is not further investigated for this work.

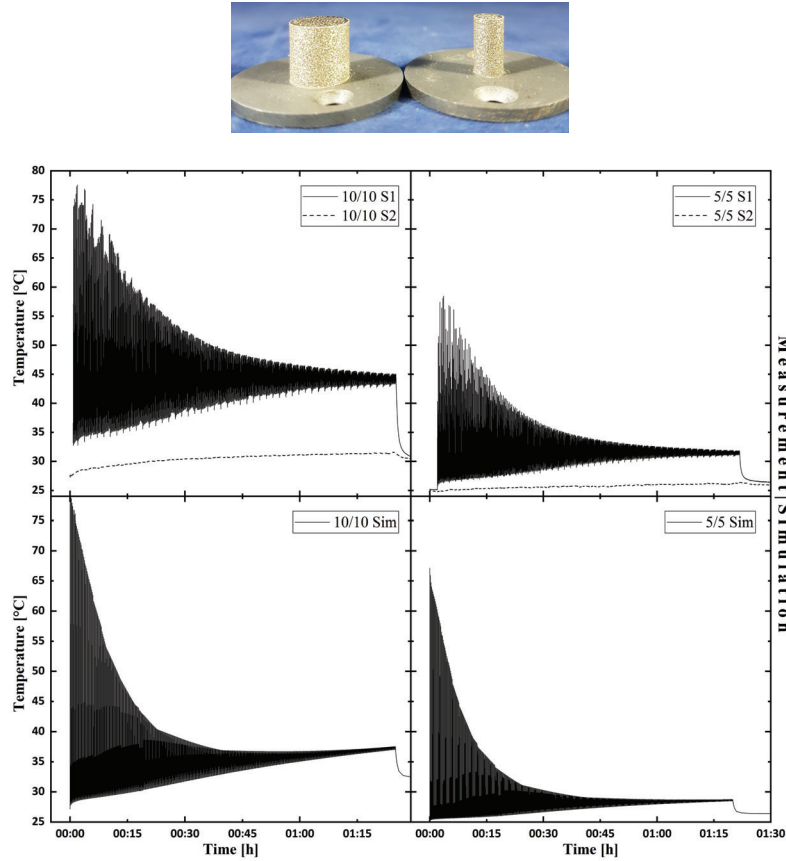


Figure 6: Temperature progression of sensor 1 (S1) 2 mm below the part and sensor 2 (S2) under the substrate plate for the build up of a 10 mm high cylinder with a diameter of 10 mm (**top left**) and 5 mm (**top right**). Simulation of both cylinders with diameter: 10 mm (**bottom left**) and 5 mm (**bottom right**).

The first comparative experiment shows the influence of part volume by comparing the benchmark cylinder ($d = 10$ mm) with a cylinder of 5 mm diameter. Thus, the ratio of volume to interface area to the substrate plate is kept constant. The results are displayed in figure 6. A similar temperature progression can be seen for the smaller cylinder with reduced peak maxima 58.5 °C, minima 25.9 °C and average final value 31.5 °C. Furthermore, an increase in deviations of the maximum values occurs due to even shorter exposure time (0.5 s).

The simulation results of the cylinder samples are evaluated at the point corresponding to the position of sensor S1 and outlined in figure 6 (bottom). From a qualitative point of view, the simulation results

are in good agreement with the measured data. The above-described fluctuation consisting of a rapid heat-up followed by a cool down phase in each layer can be found in all simulation results. Measurement and simulation show both an increase of minimal layer temperatures and a decrease in peak temperature until these values get close to each other. In a cool down phase at the end of the process the temperature decrease to a constant value.

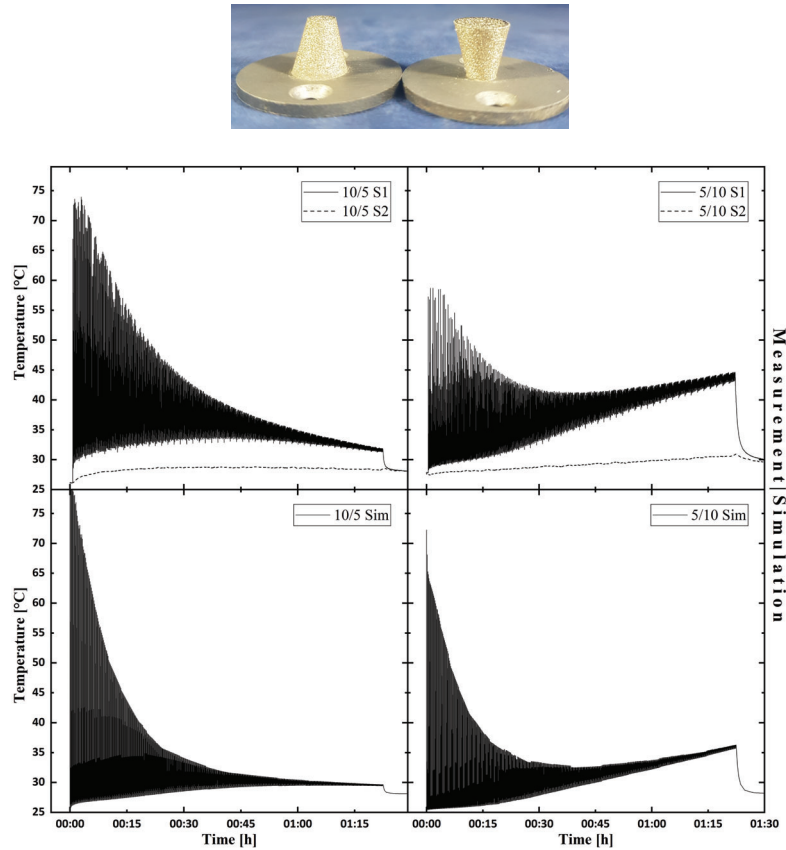


Figure 7: Temperature progression of sensor 1 (S1) 2 mm below the part and sensor 2 (S2) under the substrate plate for the build up of 10 mm high cones with a progression of the diameter of 10 → 5 mm (**top left**) and 5 → 10 mm (**top right**). Simulation of both cones with progression of the diameter: 10 → 5 mm (**bottom left**) and 5 → 10 mm (**bottom right**) .

The experimentally observed effects arising from changing the diameter between $d = 10\text{ mm}$ to $d = 5\text{ mm}$ can also be found in the simulation: The overall temperature progression is similar, but decreasing the diameter yields to lower peak, minimal and final temperatures at the end of the process. From a quantitative point of view, the comparison of measurement and simulation shows evident differences. The decrease in peak temperatures is calculated to be faster and the increase of minimal layer temperatures less than observed by measurements. This results in different temperatures at the end of the process.

Furthermore, the measured temperature decreases down to room temperature after finishing the process, whereas the simulated temperature cools down to $\theta_{\text{room}} + 1.21^\circ\text{C}$ due to boundary condition representing perfect isolation. Reasons for the differences between simulation and measurement will be discussed in section 5.

The second comparison (Figure: 7) shows the influence of energy input (\propto surface area) per exposure on the temperature progression. Therefore, two cones with same volume but reverse progression of diameter ($d_1 = 10 \rightarrow 5 \text{ mm} / d_2 = 5 \text{ mm} \rightarrow 10 \text{ mm}$) were build. Both temperature progressions start analogue to their cylindrical counterpart (Compare: 6(b/c)). The deviation from this similarity can be seen by a decrease of the average temperature ($44^\circ\text{C} \rightarrow 31.6^\circ\text{C}$) for the first and an increase ($31.6^\circ\text{C} \rightarrow 44^\circ\text{C}$) for the second sample. Hence, the results show a clear correlation between the average final temperature and the area of exposure.

The cone samples have also been simulated and the calculated temperatures at the position of S1 are shown. From a qualitative point of view, a good agreement of measured and simulated temperature progression can be observed, as in the case of cylinder geometries. In particular, differences caused by changes in geometry/orientation are reproduced. However, a quantitative comparison shows evident differences similar to the cylinders.

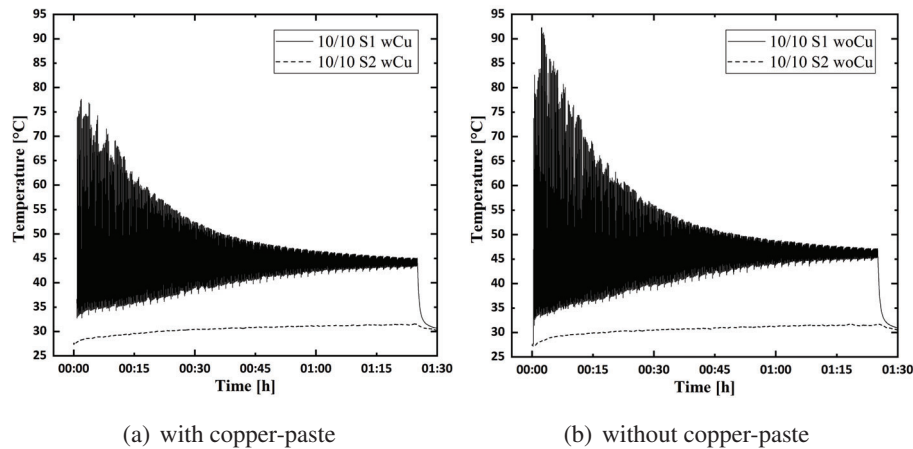


Figure 8: Temperature progression of sensor 1 (S1) 2 mm below the Part and sensor 2 (S2) under the substrate plate for the build up of a 10 mm high cylinder with (a) and without (b) copper paste as thermal bridge between substrate plate and disc

A third comparison (Figure: 8) was made to analyze the influence of the copper paste thermally bridging the sides of the disc to the substrate plate. Thus, the benchmark cylinder ($d = 10 \text{ mm}$) was built once more without using copper paste. The results show a clear impact of the missing thermal connection. An effect occurs for all samples: The maximum peak increases steadily in the first 1-3 minutes before

decreasing due to the damping effect of the increasing part height. This effect is significantly amplified for the sample without copper paste so that the increase in temperature is much faster, reaching 92.2 °C before decreasing. On the other hand, the minimum quite accurately resolves the same progression as with copper paste. This leads to the conclusion, that the copper paste decreases the time needed to deplete the energy from a single laser exposure, but the recoating time is still long enough so that the effect is not accumulating. Therefore, the copper paste is not necessary for parts of this size but could become crucial for larger part geometries.

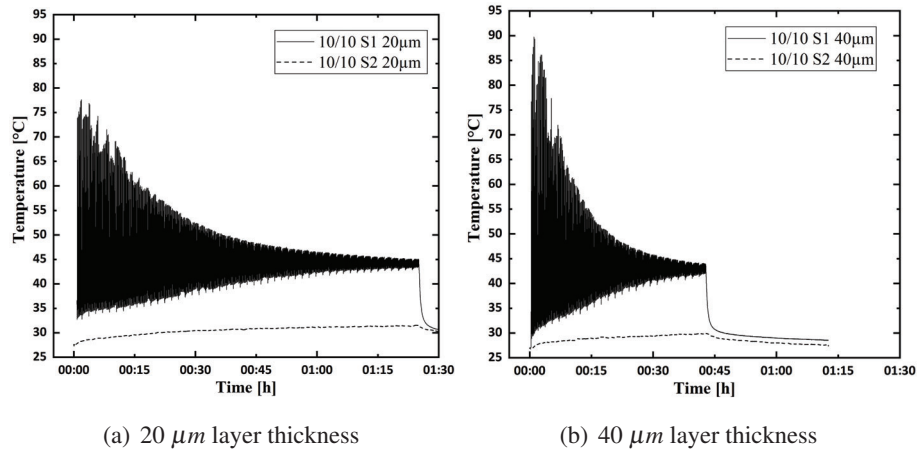


Figure 9: Temperature progression of sensor 1 (S1) 2 mm below the part and sensor 2 (S2) under the substrate plate for the build up of a 10 mm high 10 mm diameter cylinder with a layer thickness of 20 μm (a) and 40 μm (b)

For the last comparison (Figure: 9), the benchmark cylinder ($d = 10$ mm) was built with 40 μm instead of 20 μm layer height, keeping all other process parameters - laser power, laser velocity etc.- constant. Against intuitive understanding, bringing in and melting more mass leads to an increase of the initial maximum peak temperature (89.7 °C). On the contrary, the average end temperature reaches nearly the same value (43 °C). An increased peak temperature could be caused by enhanced absorption of laser energy by the additional powder. However, the matching average end temperature contradicts this assumption. Thus, further investigation is necessary to be able to create a plausible connection.

Figure 10 (left) summarizes the correlation between the cylinders with $d = 10$ mm, $d = 5$ mm and cones with $d = 10 - 5$ mm, $d = 5 - 10$ mm. The progression of the maximum temperature peaks was fitted to an exponential decay function for both cylinders and the $d = 10 - 5$ mm cone as well as to a polynomial function for the $d = 10 - 5$ mm cone. This illustration clearly shows the transition of the cones from the thermal state of one cylinder to the other. It deepens the assumption that for this setup the area of exposure mainly defines the temperature progression.

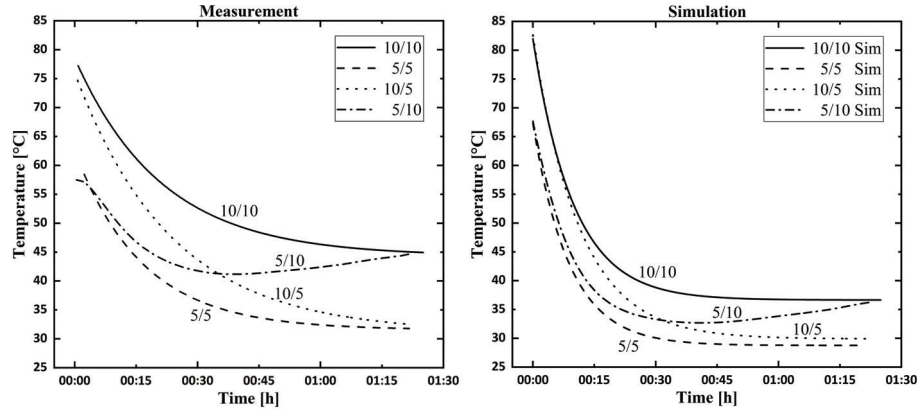


Figure 10: Fitted progression of the maximum peak temperatures of sensor 1 (S1) for cylinder with $d = 10$ mm & $d = 5$ mm and cones with $d = 10 - 5$ mm & $d = 5 - 10$ mm for measurements **left** and simulation **right**.

5. Discussion

The experiments show very insightful results. Nevertheless, a few optimizations of the setup should be made for further investigations.

The fixation of the thermocouples is a time-consuming procedure. The point weld must have good contact with the disc to ensure a decent thermal connection but also fixate the stiff wire. Since the results show a maximum temperature below $100\text{ }^{\circ}\text{C}$ a heat resistant reversible glue could be used additionally to decrease setup time between experiments.

The third comparison showed a significant influence of copper paste on the overheating effect of the disc in the first few minutes. The thermal resistance between disc and plate still poses a deviation from the regular process and should be reduced. The simulations treat disc and substrate plate as one homogeneous material. Hence, the disc heats up significantly more for the experiment than predicted by simulation. Furthermore, the simulated peak temperatures of each layer are decreasing faster than the measured ones. This can be explained by the fact that the heat conduction from the disc downwards into the substrate-plate is slower than in solid material. A simple solution could be to use the copper paste on the bottom of the disc as well and also implement a reduced thermal conductivity at the transition into the simulation.

To decrease the deviations from the maximum peak progression, an increase in temporal resolution ($< 1/s$) for the first sensor should be pursued. This, and synchronizing the measurements with the system time of the machine, could enable the analysis of single peaks and laser interaction.

The used simulation model is based on several assumptions to keep it simple, computationally efficient and usable even for larger parts. The qualitative agreement of measurement and simulation indicates its general ability to predict the global part heat-up (in particular temperatures in the substrate-plate). Nevertheless, an improvement of the model is required, since the quantitative comparison of simulated and

measured data is not satisfying yet. Therefore, it is planned to include convection boundary conditions to enable energy dissipation out of the system. This is a crucial point, especially for large parts, but it was already noticeable in the current situation. First of all, the system does not cool down to room temperature after the process ends. Additionally, in the case of cylindrical samples, the slope of the measured minimum temperatures of the layers decreases over time. In contrast, the simulated minimum temperatures produce a constant positive slope. This difference is expected to be minimized if heat dissipation out of the system is taken into account. In addition, the influence of powder and phase transformation has to be analyzed by including powder elements and considering a temperature dependent heat capacity. The used material parameters are taken from literature or generated with the help of the JMatPro software. These parameters depend e.g. on the temperature history of the material and can thus deviate from the values of the actually used material.

There are several possible influencing factors that should be analyzed in further investigations. The setup could be used for optimization studies of support structures regarding their capability to dissipate heat. A comparison of different materials, process parameters, geometries or defects should be considered as well. It could lead to a better understanding of heat dissipation mechanisms during LPBF-M. In particular materials that are very sensitive towards their thermal history, like amorphous metal, would greatly benefit from further investigations.

6. Conclusion

A new method to analyze the thermal system of LPBF-M has been presented. It enables a new perspective to look at temperature progression during the build up of small structures. The acquired data shows very high consistency in itself and is mainly influenced by the area of exposure.

Additionally, this approach can serve as a validation method for thermal simulations. It is less resource intensive and provides more reliable data compared to optical measurements from the top surface. Hence, a simulation has been stated and solved numerically. From the qualitative side, the simulation results agree well with the measurements. The characteristic progression of temperature curves, as well as the influence of different considered geometries, were predicted well. Finally, several approaches for further improvement of simulation as well as for experimental setup were discussed.

The presented method has shown the potential to enhance the insight of LPBF-M both through measurement and simulation.

References

- [1] Acatech - National Academy of Science and Engineering, German National Academy of Sciences Leopoldina, and Union of the German Academies of Sciences and Humanities. *Additive Manufacturing: Statement of Acatech*. Munich, 2017.
- [2] VDI Verein Deutscher Ingenieure e. V. Handlungsfelder - additive fertigungsverfahren. 2016.
- [3] EFI - Expertenkommission Forschung und Innovation. Research, innovation and technological performance in germany. 2015.
- [4] Wohlers Associates. *Wohlers Report 2018: 3D Printing and Additive Manufacturing State of the Industry*. 2018.
- [5] Yasa E., Kempen K., Kruth J.-P. Microstructure and mechanical properties of maraging steel 300 after selective laser melting. 2010.
- [6] Hyo Yun Jung, Su Ji Choi, Konda G. Prashanth, Mihai Stoica, Sergio Scudino, Seonghoon Yi, Uta Kühn, Do Hyang Kim, Ki Buem Kim, and Jürgen Eckert. Fabrication of fe-based bulk metallic glass by selective laser melting: A parameter study. *Materials & Design*, 86:703–708, 2015.
- [7] Thomas G. Spears and Scott A. Gold. In-process sensing in selective laser melting (slm) additive manufacturing. *Integrating Materials and Manufacturing Innovation*, 12:683, 2016.
- [8] Marco Grasso, Vittorio Laguzza, Quirico Semeraro, Bianca Maria Colosimo. In-process monitoring of selective laser melting: Spatial detection of defects via image data analysis. *Journal of Manufacturing Science and Engineering*, (139), 2016.
- [9] Joschka Zur Jacobsmühlen, Stefan Kleszczynski, Dorian Schneider, and Gerd Witt. High resolution imaging for inspection of laser beam melting systems. In *IEEE International Instrumentation and Measurement Technology Conference (I2MTC) 2013*, pages 707–712, 2013.
- [10] Diego de Moraes and Aleksander Czekanski. Parametric thermal fe analysis on the laser power input and powder effective thermal conductivity during selective laser melting of ss304l. *Journal of Manufacturing and Materials Processing*, 2(3):47, 2018.
- [11] Lien Chin Wei, Lili E. Ehrlich, Matthew J. Powell-Palm, Colt Montgomery, Jack Beuth, and Jonathan A. Malen. Thermal conductivity of metal powders for powder bed additive manufacturing. *Additive Manufacturing*, 21:201–208, 2018.
- [12] A.V. Gusarov, T. Laoui, L. Froyen, V.I. Titov. Contact thermal conductivity of a powder bed in selective laser sintering. *International Journal of Heat and Mass Transfer*, (46), 2003.
- [13] Marco Grasso and Bianca Maria Colosimo. Process defects and in situ monitoring methods in metal powder bed fusion: a review. *Measurement Science and Technology*, 28(4), 2017.
- [14] Emmanuel Rodriguez, Jorge Mireles, Cesar A. Terrazas, David Espalin, Mireya A. Perez, and Ryan B. Wicker. Approximation of absolute surface temperature measurements of powder bed fusion additive manufacturing technology using in situ infrared thermography. *Additive Manufac-*

turing, 5:31–39, 2015.

- [15] Yiğit M. Arisoy, Luis E. Ciales, and Tuğrul Özel. Modeling and simulation of thermal field and solidification in laser powder bed fusion of nickel alloy in625. *Optics & Laser Technology*, 109:278–292, 2019.
- [16] Shawn Moylan, Eric Whitenon, Brandon Lane, and John Slotwinski. Infrared thermography for laser-based powder bed fusion additive manufacturing processes. AIP Conference Proceedings, pages 1191–1196. AIP Publishing LLC, 2014.
- [17] H. Krauss. *Qualitätssicherung beim Laserstrahlschmelzen durch schichtweise thermografische In-Process-Überwachung: Dissertation TU Munich*. Herbert Utz Verlag, 2017.
- [18] A. J. Dunbar, E. R. Denlinger, J. Heigel, P. Michaleris, P. Guerrier, R. Martukanitz, and T. W. Simpson. Development of experimental method for in situ distortion and temperature measurements during the laser powder bed fusion additive manufacturing process. *Additive Manufacturing*, 12:25–30, 2016.
- [19] Jamasp Jhabvala, Eric Boillat, Thibaud Antignac, and Rémy Glardon. On the effect of scanning strategies in the selective laser melting process. *Virtual and Physical Prototyping*, 5(2):99–109, 2010.
- [20] P. Peyre, P. Aubry, R. Fabbro, R. Neveu, and A. Longuet. Analytical and numerical modelling of the direct metal deposition laser process. *Journal of Physics D: Applied Physics*, 41(2), 2008.
- [21] EOS GmbH. *Material data sheet - EOS GmbH EOS StainlessSteel GP1*, 2009.
- [22] Peter Knabner. *Numerical Methods for Elliptic and Parabolic Partial Differential Equations*. Texts in Applied Mathematics, 44. 2003.
- [23] Klaus-Jürgen Bathe. *Finite element procedures*. [2. print] edition, 1996.
- [24] Christian Kober, Hong Xu, Nils Keller, and Vasily Ploshikhin. Creating a layer based mesh for additive manufacturing simulation. DVS Media, 2013.
- [25] Ovako Group AB. *Material data sheet Steel grade C45*, 2019.